Mechanical Design of HD2, a 15 T Nb_3Sn Dipole Magnet with a 35 mm Bore

P. Ferracin, S. E. Bartlett, S. Caspi, D. R. Dietderich, S. A. Gourlay, A. R. Hafalia, C. R. Hannaford, A. F. Lietzke, S. Mattafirri, A. D. McInturff, and G. L. Sabbi

***Abstract*— After the fabrication and test of HD1, a 16 T Nb_3Sn dipole magnet based on flat racetrack coil configuration, the Superconducting Magnet Program at Lawrence Berkeley National Laboratory (LBNL) is developing the Nb_3Sn dipole HD2. With a dipole field above 15 T, a 35 mm clear bore, and nominal field harmonics within a fraction of one unit, HD2 represents a further step towards the application of block-type coils to high-field accelerator magnets. The design features tilted racetrack-type ends, to avoid obstructing the beam path, and a 4 mm thick stainless steel tube, to support the coil during the pre-loading operation. The mechanical structure, similar to the one used for HD1, is based on an external aluminum shell pre-tensioned with pressurized bladders. Axial rods and stainless steel plates provide longitudinal support to the coil ends during magnet excitation. A 3D finite element analysis has been performed to evaluate stresses and deformations from assembly to excitation, with particular emphasis on conductor displacements due to Lorentz forces. Numerical results are presented and discussed.**

***Index Terms*—Nb_3Sn, dipole magnet**

I. Introduction

In the last 10 years, the LBNL superconducting magnet program has fabricated and tested high-field dipole magnets based on Nb_3Sn coils of three different configurations: shell-type (D20, 13 T, 1996) [1]; dual-bore common coil (RD3b, 14.5 T, 2001) [2]; single-bore block-coil (HD1b, 16.1 T, 2004) [3]. HD1 achieved a 16 T field in an 8 mm bore using flat racetrack coils. The main goals for HD2 are increasing the clear bore size to 35 mm while maintaining a dipole field above 15 T. The HD2 conceptual design was presented in [4]. The magnet uses a simple block-coil configuration with tilted ends. The coil layout and winding method are derived from the D10 dipole, the first Nb_3Sn magnet developed by the LBNL program [5]. A similar coil configuration was also adopted by the Texas A&M program for the design of a 16 T dipole featuring a system of intercepts to limit the coil stress [6].

In this paper, the design features of HD2 are reviewed, and a detailed mechanical analysis of the magnet straight section and end regions is presented.

Manuscript received September 20, 2005. This was supported by the Director, Office of Energy Research, Office of High Energy and Nuclear Physics, High Energy Physics Division, U. S. Department of Energy, under Contract No. DE-AC02-05CH11231.

All authors are with Lawrence Berkeley National Lab, Berkeley, CA 94720 USA (phone: 510-486-4630; fax: 510-486-5310; e-mail: pferracin@lbl.gov).

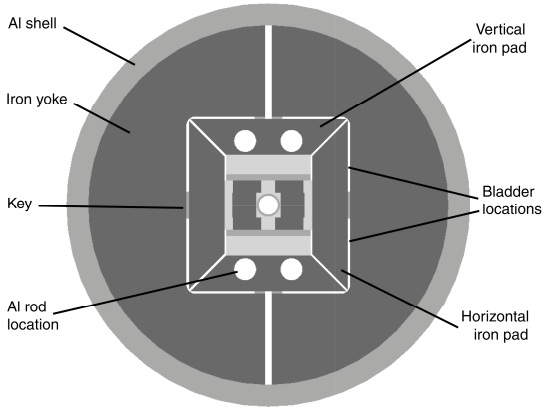

Fig. 1. HD2 magnet cross-section and main mechanical support elements.

II. Magnet Design

A. Cross-Section Design

The HD2 design (Fig. 1) features two double-layer modules, each one wound from a continuous length of cable. A coil design iteration was performed following the fabrication and evaluation of prototype cables, and preliminary winding tests. The selected cable design uses 51 strands of 0.8 mm diameter. With respect to the previous version [4], the revised design has one less turn in each layer: 27 turns in layer 1 (facing the magnet mid-plane) and 32 turns in layer 2. The coil aperture is approximately square shaped, with a side of 45 mm. A 3 mm thick mid-plane spacer separates the two coil modules. The winding pole (with a minimum winding radius of 12.75 mm in layer 2) has a round cutout which is used to assemble the coil modules around a 4 mm thick stainless steel tube, providing a 35 mm diameter clear bore.

Updated magnet parameters are given in Table I: assuming the same strand properties of HD1, the magnet generates a maximum bore field of 15.4 T (4.2 K). The peak field in the conductor is 16.1 T. At full field, all design harmonics are below 0.5 units at a 10 mm reference radius.

The HD2 mechanical structure is similar to the one designed for HD1 [7]. The coil is supported by horizontal and vertical pads. Vertical pushers and horizontal rails transfer the load from the pads to the coils. The coil-pad sub-assembly is surrounded by iron yokes and an aluminum cylinder (shell). A 5 mm gap between pads and yokes provides room for 4

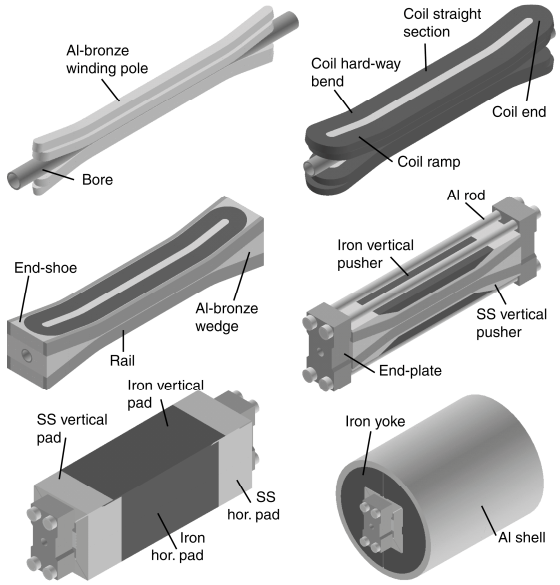

Fig. 2. HD2 coil module and support structure.

TABLE I
CONDUCTOR AND MAGNET PARAMETERS

Parameter	Unit	
Strand diameter	mm	0.8
Strand Ic (16 T, 4.2K)	A	322
Cu/Sc ratio		0.94
No. strands		51
Cable height (bare)	mm	21.86
Cable thickness (bare)	mm	1.40
Insulation thickness (h/v)	mm	0.11/0.11
No. turns/quadrant (layer 1)		27
No. turns/quadrant (layer 2)		32
Short sample current	kA	15.6
Maximum dipole field	T	15.4
Coil peak field	T	16.1
Stored energy	MJ/m	0.87
Inductance	mH/m	7.3
Fx / Fy layer 1 (per quadrant)	MN/m	+ 2.5 / - 0.4
Fz layer 1 (per quadrant)	kN	85
Fx / Fy layer 2 (per quadrant)	MN/m	+ 3.4 / - 2.0
Fz layer 2 (per quadrant)	kN	114

bladders, 70 mm wide. During assembly, the bladders are inserted and pressurized. The generated clearance is locked with 2 horizontal interference keys, and the bladders are deflated and removed, following the procedure described in [8]. During cool-down, the difference between the thermal contraction of the aluminum shell and that of the iron yoke produces an increase of tension in the shell and, consequently, of horizontal compression of the coils. Along the vertical direction, four keys provide a bridge between yoke and pads, at same time limiting the yoke bending and vertically pre-stressing the coils.

B. End Design

The coil end geometry (Fig. 2, top left) was also revised based on tests of prototype cables. In particular, the radius of the hard-way bend was significantly increased (to about 380 mm). The new design also decouples the hard-way and easy-way bends for the transition between the two layers. After the hard-way bend, a racetrack configuration is recovered on a plane inclined by 10^o with respect to the magnet axis. The straight parts of the racetrack end ("ramps") are respectively 82 mm and 100 mm long in layer 1 and layer 2. The ramps are followed by easy-way bends ("ends"). The total coil length is 876 mm for a straight section of 400 mm.

Details of the coil support elements are shown in Fig. 2. An aluminum-bronze wedge encompasses the bore in the end region and provides vertical support to the ramp. The volume delimited by the coil and the vertical pads is filled with a vertical pusher, composed by an iron part, which enhances the field in the straight section, and a stainless steel part, which provides a continuous contact surface along the entire coil length. Aluminum-bronze rails cover the coil sides, and transfer the horizontal load from the pads to the conductor (there is no contact between horizontal pads and wedge). Both the vertical and horizontal pads are divided in an iron part and a stainless steel part, whose axial lengths have been optimized in order to reduce field and stresses in the coil ends. Similarly to previous LBNL magnet designs [7], longitudinal support of the ends is accomplished with four axial rods. The rods, with a radius of 18.5 mm, are inserted through holes provided over the full length of the vertical pads and bolted to two 90 mm thick stainless steel end-plates. A tensioning fixture applies the initial pre-tension to the rods, which increases during cool-down because of the high thermal contraction of the aluminum. The axial force is transferred to the coil layers through a one-piece end-shoe.

III. MECHANICAL ANALYSIS

Both 2D and 3D finite element models were implemented in ANSYS to perform the mechanical analysis. The 2D model of the magnet cross-section was aimed at defining the main component dimensions and the bladder/key assembly procedure, as well as investigating coil stresses in the straight section. The 3D model (Fig. 3) was focused on the mechanical behavior of the complete magnet structure, with particular emphasis on coil pre-stress homogeneity along the axial direction, and required axial support to minimize conductor motion. Both perfect sliding and friction contact (μ = 0.2) between coil and structural components were analyzed.

We present the analysis results as follows: in Fig. 4 we plot the tension in shell and rods during assembly, cool-down, and excitation. For both components, the room temperature tension (end of the assembly) has been chosen so that the coil is maintained under compression during all magnet operations (we point out that epoxy impregnation may provide further margin against separation at the coil-pole interface). To verify this assumption, we plot the model results along two different paths. The first path (transverse path), used in Fig. 5 and Fig. 6, provides the coil horizontal stress in the central cross-section of the magnet (z = 0). The path is located at the middle of each layer, moving from the inner coil surface (facing the pole) to the outer coil surface (facing the rails). The second path (longitudinal path), used in Fig. 7 and Fig. 8, provides the contact pressure between coil and winding pole along the

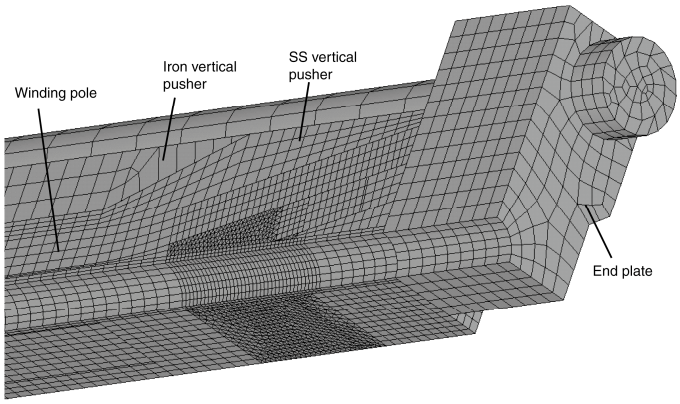

Fig. 3. 3D finite element model of the end region.

magnet axial direction. Four regions have been considered: straight section, hard-way bend, ramp, and ends. Also in this case, the path is located at the middle of the contact area between each coil layer and winding pole, moving from magnet center to end region.

A. Assembly

The room temperature stress conditions are characterized by a rod tension of 150-170 MPa and a shell tension of 60 MPa (Fig. 4). In order to pre-tension the shell to such a level, the bladders are pressurized to 45 MPa, and a clearance of 800 μm is generated between yoke and horizontal pads to insert the keys. At the end of the assembly the coil is compressed to 40-45 MPa and 55-65 MPa, respectively in layer 1 and layer 2 (Fig. 5-6). This stress non-uniformity between the two layers is related to the geometry of the winding pole: the part of the pole facing layer 1 is less rigid, since it includes the cutout for the bore tube, which deforms when compressed by the pads. On the other hand, the part facing layer 2 is solid, and constitutes a more rigid boundary for the conductors during the pre-stressing phase.

Regarding the evolution of coil stresses and contact pressure, no significant variations are observed along respectively the transverse (Fig. 5-6) and longitudinal path (Fig. 7-8).

B. Cool-down

After cool-down, the shell reaches 150 MPa, while the rods present a different mechanical response depending on the assumed friction coefficient (Fig. 4). If the rods can shrink freely against the coil (perfect sliding condition), the stress increases to 270 MPa. If friction is included between coil and structural components, the rod contraction is limited by the mechanical structure, and the stress rises to 300 MPa.

The coil compression after cool-down is 120-130 MPa in layer 1 and 150-170 MPa in layer 2, with small variations along the transverse path (Fig. 5-6). Along the longitudinal path, the contact pressure between coil and pole is characterized by a significant variation (Fig. 7-8). Following the straight section, layer 1 features an increase of compression in the hard-way bend and the ramp, where the winding pole raises vertically over the bore and becomes completely solid. Consequently, layer 2 undergoes a stress reduction, enhanced by the presence of a stainless steel (higher thermal contraction) horizontal pad.

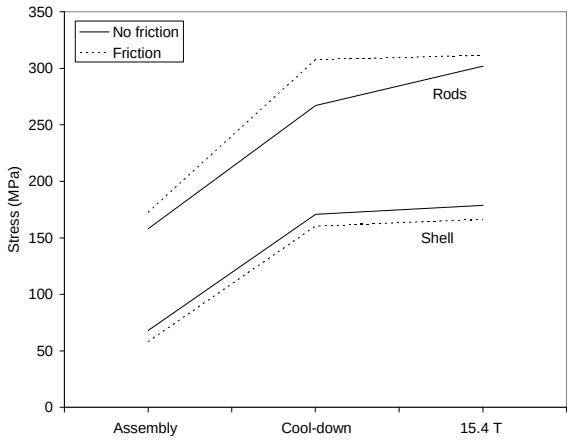

Fig. 4. Shell and rod stress (tension) during magnet assembly, cool-down and excitation.

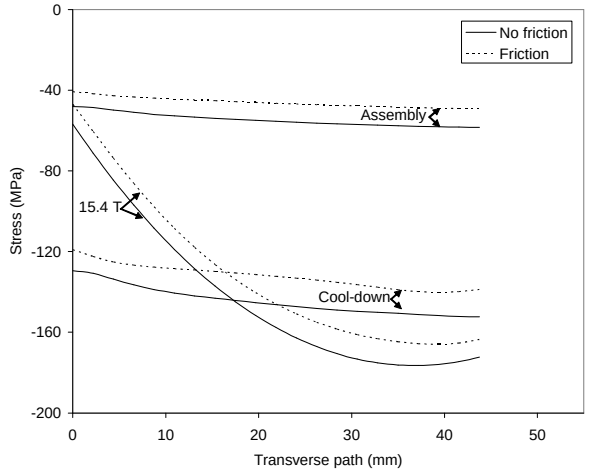

Fig. 5. Horizontal stress in coil layer 1: results are given along the transverse path, located at the middle of layer 1 (y = 12.5 mm), and moving from the coil surface facing the pole (x = 0 mm) to the one facing the rails (x = 43.7 mm).

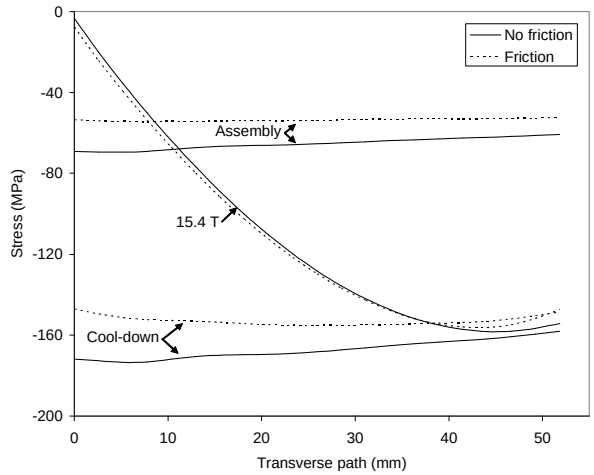

Fig. 6. Horizontal stress in coil layer 2: results are given along the transverse path, located at the layer middle (y = 34.6 mm), and moving from the coil surface facing the pole (x = 0 mm) to the one facing the rails (x = 51.8 mm)

In the end region, the rods ensure a contact pressure of about 55 MPa and 75 MPa between coil and pole, respectively in layer 1 and layer 2.

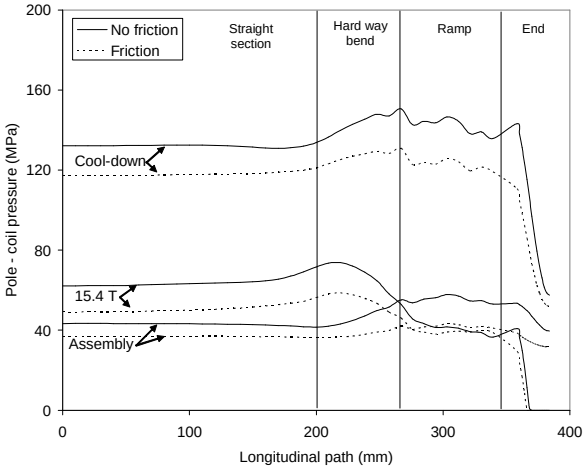

Fig. 7. Contact pressure between winding pole and coil layer 1: results are given along the longitudinal path, located at the middle of the layer, and moving from the straight section center (z = 0 mm) to the end (z = 384 mm).

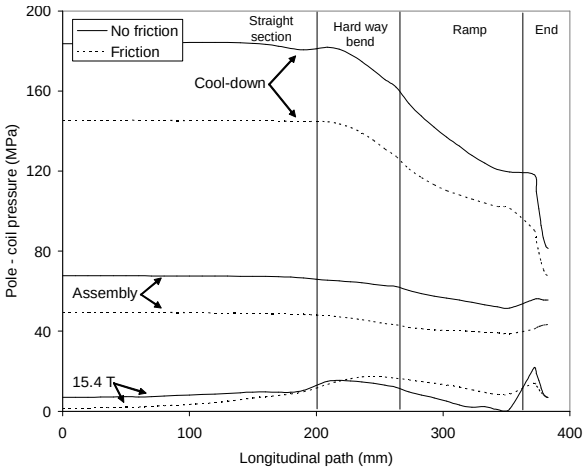

Fig. 8. Contact pressure between winding pole and coil layer 2: results are given along the longitudinal path, located at the middle of the layer, and moving from the straight section center (z = 0 mm) to the end (z = 383 mm).

C. Excitation

Under the effect of Lorentz forces, which tend to separate the coil from the pole, the models predict a tension increase of 7 MPa for the shell, and of 5 MPa for the rods, assuming friction contact. If perfect sliding is considered, the rod stress change rises to 30 MPa, corresponding to a larger motion when the coil is free to slide with respect to the surrounding structure.

The level of coil pre-stress reached after cool-down ensures that, when Lorentz forces are applied, no separation occurs at the coil-pole interface (15.4 T curves in Fig. 5-6). In particular, layer 1, characterized by lower electromagnetic forces (Table I), maintains at full field about 50 MPa of pre-stress, while layer 2 remains in light contact with the pole. On the rail side, the coil reaches a peak stress of about 180 MPa in layer 1, which reduces to about 160 MPa when friction is included.

In the end region, the pole unloads to 7 MPa in layer 2, while separation starts occurring on layer 1 (15.4 T curves in Fig. 7-8). The details of the expected conductor motion in the ends are shown in Fig. 9: the gaps between coil and pole are plotted

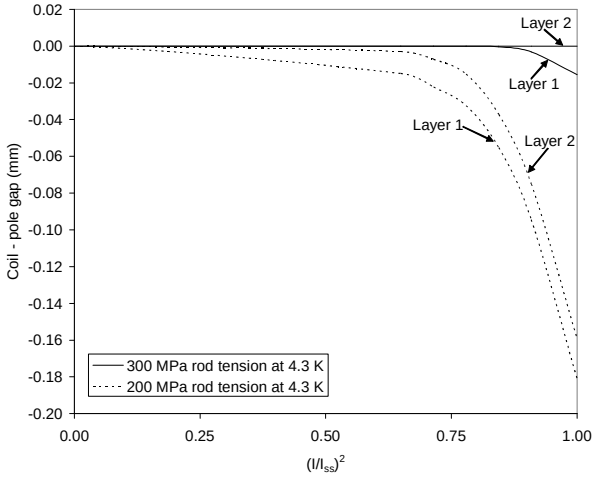

Fig. 9. Gaps between coil and pole for two different levels of rod tension.

as a function of the fraction of Lorentz force with respect to the short sample value $(I/I_{ss})^2$. Two different axial loading conditions are investigated: the solid lines represent the computed gap relative to the conditions presented in Fig. 7-8, while the dashed lines describe a situation where the rod tension after cool-down is reduced by 30%.

The results confirm the importance of the axial loading, which can significantly limit the conductor tendency to lift from the pole under the action of the longitudinal Lorentz forces.

IV. Conclusions

A review of the HD2 magnet design has been presented, with a detailed analysis of its mechanical behavior. The magnet generates a field of 15.4 T at 4.2 K in a 35 mm bore, and requires coil pre-stress of the level of 180 MPa in the straight section.

The support structure provides uniform coil pre-stress along the magnet axial length, and minimizes the conductor motion in the end regions.

References

[1] A. McInturff, *et al.*, "Test Results for a High Field (13 T) Nb_3Sn Dipole", in *Proc. Pac-97*, Vancouver, 1997, pp 3212-3214.

[2] R. Benjegerdes, *et al.*, "Fabrication and Test Results of a High Field, Nb_3Sn Superconducting Racetrack Dipole Magnet", *Proc. Pac-01*, Chicago, 2001, pp 208-210.

[3] A. F. Lietzke, *et al.*, "Test Results of HD1b, an Upgraded 16 T Nb_3Sn Dipole Magnet", *IEEE Trans. Appl. Superconduct*., Vol. 15, no. 2, pp. 1123-1127, June 2005.

[4] G. Sabbi, *et al.*, "Design of HD2: a 15 T Nb_3Sn Dipole with a 35 mm Bore", *IEEE Trans. Appl. Superconduct.*, Vol. 15, no. 2, pp. 1128-1131, June 2005.

[5] C. Taylor, *et al.*, "A Nb_3Sn Dipole Magnet Reacted after Winding", *IEEE Trans. Magn.*, Vol. MAG-21, no. 2, pp. 967-970, March 1985.

[6] T. Elliott, *et al.*, "16 Tesla Dipole Development at the Texas A&M University", *IEEE Trans. Appl. Superconduct.* Vol 7, No. 2, pp. 555-557, June 1997.

[7] P. Ferracin, *et al.*, "Mechanical Analysis of the Nb_3Sn Dipole Magnet HD1", *IEEE Trans. Appl. Superconduct.*, Vol. 15, no. 2, pp. 1119-1122, June 2005.

[8] S. Caspi, *et al.*, "The Use of Pressurized Bladders for Stress Control of Superconducting Magnets", *IEEE Trans. Appl. Superconduct*., vol. 11, no. 1, pp. 2272-2275, March 2001.